Understanding the Thermal Stability of Silver Nanoparticles Embedded in a-Si

Anna L. Gould,[†,‡] Shima Kadkhodazadeh,[§] Jakob B. Wagner,[§] C. Richard A. Catlow,[†,‡] Andrew J. Logsdail,*[,‡] and Marcel Di Vece*[,‖]

[†]UK Catalysis Hub, Research Complex at Harwell, Rutherford Appleton Laboratory, Harwell, Oxfordshire OX11 0FA, U.K.

[‡]Kathleen Lonsdale Materials Chemistry, Department of Chemistry, University College London, 20 Gordon Street, London, WC1H 0AJ, U.K.

[§]Centre for Electron Nanoscopy, Technical University of Denmark, DK-2800 Kongens Lyngby, Denmark

[‖]Nanophotonics—Physics of Devices, Debye Institute for Nanomaterials Science, Utrecht University, Princetonplein 5, 3584 CC Utrecht, The Netherlands

S *Supporting Information*

ABSTRACT: The inclusion of silver plasmonic nanoparticles in silicon is highly relevant for photovoltaics as it may enhance optical absorption. We report an investigation of the stability of such pristine silver nanoparticles embedded in a-Si upon heat treatment. We have investigated the morphological changes via *in situ* and *ex situ* high-resolution and high-angle annular dark-field scanning transmission electron microscopy (HRTEM and HAADF STEM). The melting of Ag particles and subsequent interdiffusion of Ag and Si atoms are strongly related to the size of the Ag nanoparticles, as well as the presence of surface imperfections. Partial voids in the amorphous-Si framework are formed where sections of the Ag nanoparticles are found preferentially to diffuse away due to geometric instability. Computational simulations using ensemble molecular dynamics confirm the experimental results: the structural properties of the amorphous-Si environment are important as well as incomplete packing of the Ag nanoparticle surfaces. These factors affect the melting temperature, causing some parts of the Ag nanoparticles to dissolve preferentially and other areas to remain stable at high temperatures.
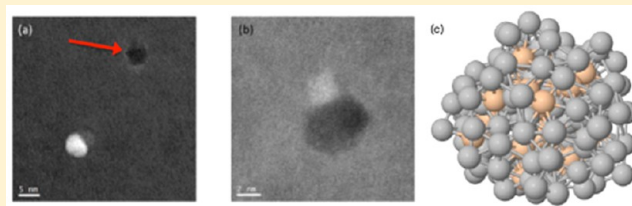
INTRODUCTION

The deliberate encapsulation of metallic nanostructures, particularly nanoparticles (NPs), inside semiconducting materials has shown promise for thin-film photovoltaic applications[1−5] and in the development of biomolecule imaging techniques, such as surface-enhanced Raman scattering,[6−9] due to near-field plasmonic absorption induced by the embedded NPs.[1,4] In the development of thin-film solar cells, silver has typically been used as a back contact for materials such as crystalline- and amorphous-silicon (c-Si and a-Si, respectively).[10−13] However, the increasing need to minimize manufacturing costs requires a reduction in the amount of high-quality semiconductor material used in a solar cell while maintaining high efficiency.[5] Therefore, the embedding within silicon of silver NPs (Ag NPs), and bimetallic composites, is currently of interest due to the strong, tunable plasmonic absorption by the NP in the visible region of the solar radiation spectrum.[14−17]

To maximize the efficiency of embedded Ag NPs in photovoltaic applications, an understanding of the size, shape, and stability of the NPs is necessary.[5,16,18] Previous work has shown that direct imaging using electron microscopy provides quantitative information about the size and shape of NPs,[19−23] while optical characterization illustrates the tunability of the absorption spectrum.[18,24,25] Knowledge of the stability of the

embedded Ag NPs, however, is limited to hypotheses made from studies carried out on bulk interfaces, where diffusion of Ag in Si materials is found to be slow,[26,27] which is corroborated by computational studies of the large energy barriers for the penetration of Ag atoms into c-Si (111) surfaces.[28,29] In this article, we look to advance this field by reporting our observations on the stability of pristine Ag NPs encapsulated in a-Si, with respect to size and structure, when heated using *in situ* high-resolution transmission electron microscopy (HRTEM). We find evidence of correlations between the size of the Ag NPs, as well as the presence of surface imperfections on the Ag NPs, and the interdiffusion of Ag and Si atoms. Our results are illuminated via computational simulations using ensemble molecular dynamics, where the properties of the a-Si environment are also shown to be influential. We also report the formation of partial voids in the a-Si framework, where sections of the Ag NP are found to diffuse away preferentially due to geometric instability.

METHODOLOGY

Experiment. Ag NPs and a-Si composites were produced in a dedicated vacuum system that contains a NC200U-B cluster source (Oxford Applied Research)[30,31] and a magnetron sputter source for thin-film deposition. The cluster and sputter sources had a background pressure of $\sim 10^{-8}$ mbar and are connected via a central chamber such that samples can be transferred while maintaining vacuum conditions of $\sim 10^{-5}$ mbar during sample transport. The composite systems of Ag NPs and a-Si, henceforth referred to as Ag-a-Si, were produced via a three-step protocol: (i) deposition of an a-Si layer on a SiN TEM grid; (ii) deposition of the Ag NPs, produced with a DC magnetron power of 30 W using Ar plasma and a 99.99% pure Ag target; (iii) deposition of another a-Si layer, effectively encapsulating the Ag NPs. The specimens, schematically represented in Figure 1, were loaded
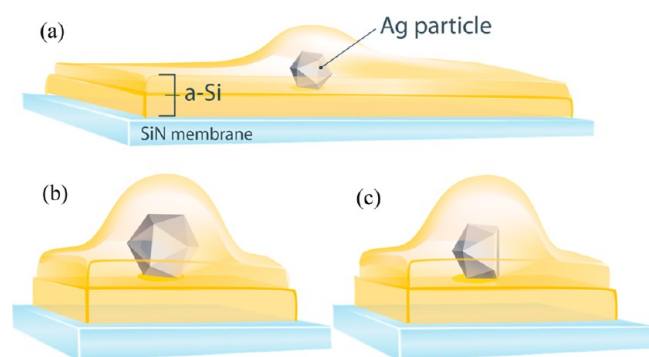
Figure 1. Schematic representation of the a-Si embedded Ag nanoparticles: (a) Sample S1, nominally 15 nm a-Si/layer embedding NPs with an average diameter of 9.4 ± 1.2 nm. (b) Sample S2, nominally 35 nm a-Si/layer embedding NPs with an average diameter of 31.9 ± 10.0 nm. (c) Sample S2 after partial atomic detachment during annealing.

into a Gatan heating holder and heated *in situ* inside an aberration-corrected FEI Titan microscope from room temperature (RT, 293 K) to a temperature, T, of 1173 K, in incremental temperature steps of 50 K. HRTEM images of the NPs were

acquired *in situ* during the thermal treatment, as well as at RT pre- and postheating. Postheating images were also acquired using high-angle annular dark field scanning TEM (HAADF STEM). It is expected that a thin oxide film forms on the a-Si surface when the sample is exposed to air, e.g., when transferred to the microscope; electron energy loss spectroscopy (EELS) measurements show the presence of 4−5% oxygen in the a-Si film. The encapsulation of the Ag NPs, however, ensures that they remain ultraclean, and no silver oxide is formed.

Computational Simulations. Isothermal−isobaric (NPT) ensemble molecular dynamics calculations were performed to complement our experimental work, simulating the annealing of Ag NPs embedded in a-Si; details of the settings and parameters used are provided in the SI. The a-Si models were created by subjecting a bulk Si supercell, containing 8000 Si atoms, to a rapid heat/quench cycle as discussed in the SI. The Ag NPs were then inserted at the center of the a-Si supercell, with all Si atoms within 1.7 Å of the Ag NP removed, creating the composite Ag-a-Si systems; for gas-phase calculations the same unit cells were used only with all the bulk Si atoms removed. Then, following thermal equilibration, the composite systems were annealed from $T = 0$ K to $T = 1000$ K in 10 K intervals, at a rate of 10 K/10 ps, using a time step (Δt) of 0.001 ps (i.e., 10 000 steps at each T). An ensemble was achieved by repeating the above process ten times, for each necessary calculation, with different random number seeds, and the results are then reported as an average over each ensemble unless explicitly stated otherwise.

RESULTS AND DISCUSSION

Two samples were studied experimentally, henceforth named S1 (nominally 15 nm a-Si/layer, Figure 1a) and S2 (nominally 35 nm a-Si/layer, Figure 1b), with the preheating HRTEM examination showing Ag NPs with a mean diameter (d) of 9.4 ± 1.2 and 31.9 ± 10.0 nm, respectively (measurements taken from 15 NPs in each case). Figure 2a presents a preheating HRTEM image of a Ag NP in S1 with $d \approx 8$ nm. The fast Fourier transform (FFT) pattern of the image (Figure 2b) reveals that the particle is not a single crystal but contains multiple twinning planes joining (111) faces, as highlighted with white arrows,
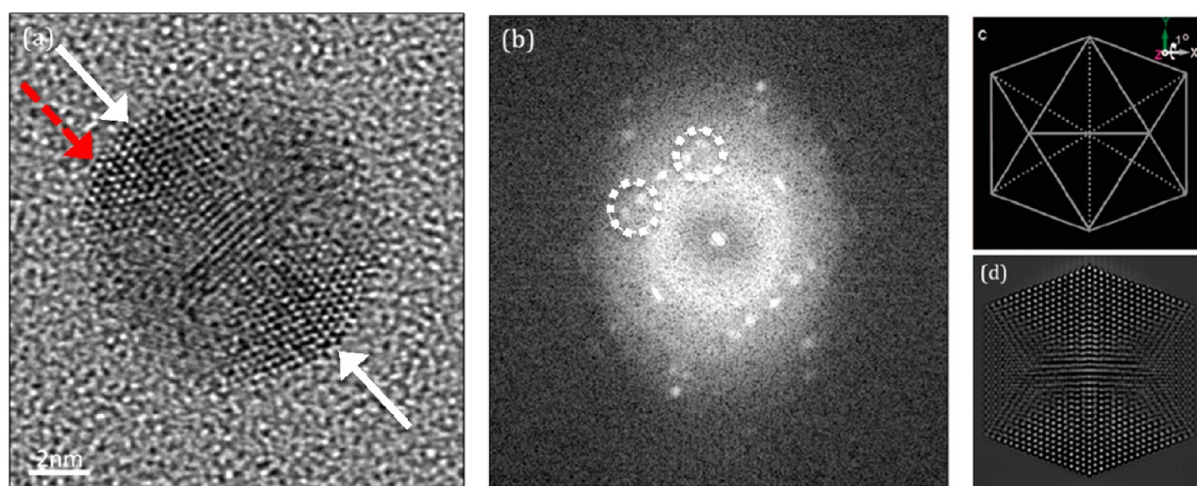
Figure 2. (a) HRTEM image of a silver nanoparticle embedded in a-Si (Sample S1), acquired at room temperature (293 K), with twinning planes and incomplete packing of surface atoms identified by white and red arrows, respectively, and (b) the corresponding FFT, where the encircled spots correspond to the twinning of crystal planes. Comparable HRTEM images of an icosahedron are presented: (c) schematic of an icosahedral geometry and (d) corresponding simulated HRTEM image for the icosahedral morphology. Images (c) and (d) are reprinted with permission from ref 32. Copyright 2009 American Chemical Society.
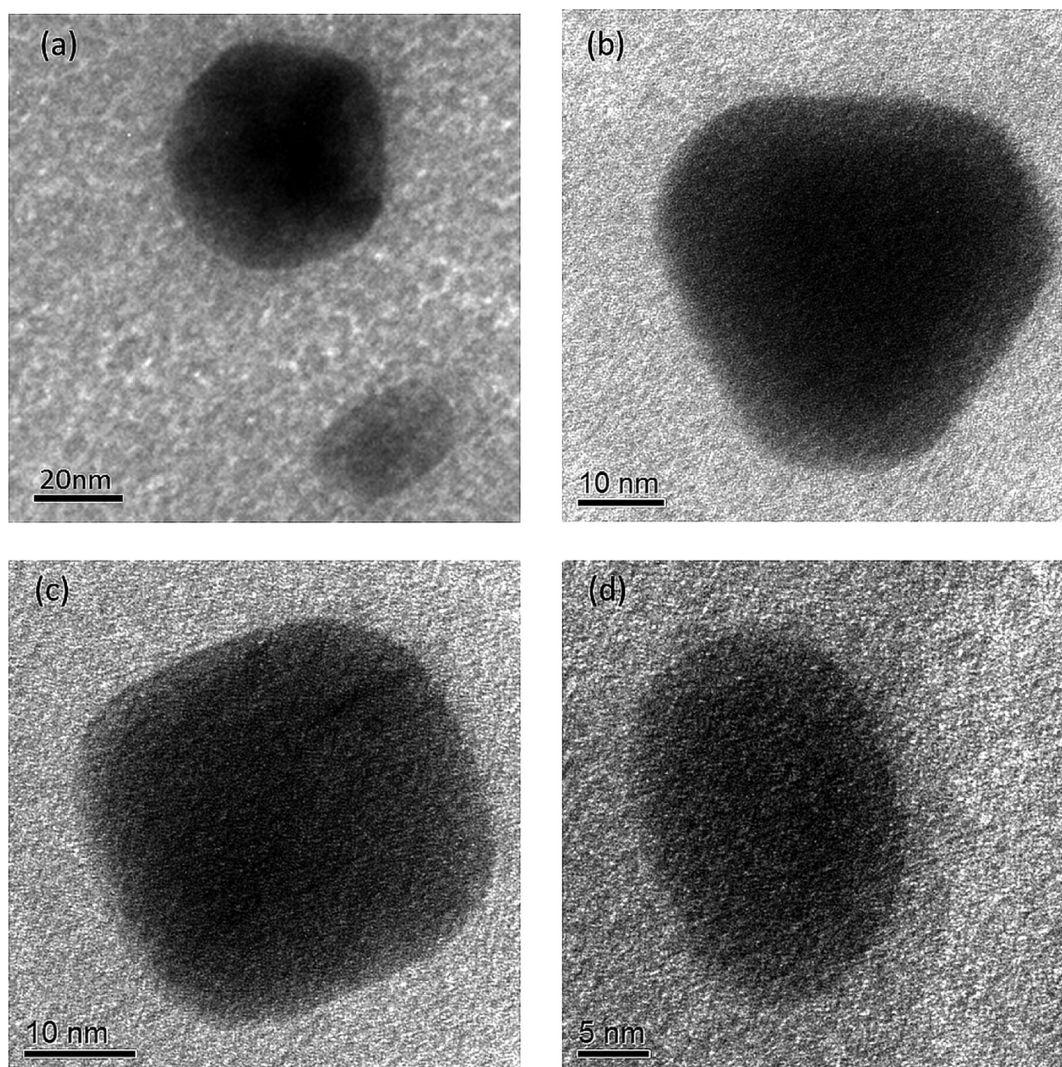
Figure 3. Bright-field TEM images showing examples of the various nanoparticle shapes observed in Sample S2.

which was observed consistently for NPs in S1, with additional HRTEM images and discussion provided in the Supporting Information (SI). Comparing these images with simulated HRTEM images of Fe NPs[32] leads us to conclude that the silver NPs in S1 have an icosahedral (Ih) structural motif, which is a polyhedron with 20 (111) faces. The predominant observation of Ih structures for the NPs in S1 is in contrast to the gas-phase theoretical predictions, where Ih motifs are favored for $d < 2$ nm, due to their close to spherical geometry and subsequent low surface area, whereas decahedral and truncated octahedral are more stable when $d > 2$ nm.[33,34] We conclude, therefore, that the larger of the observed Ih-structured Ag NPs are likely to be stabilized by the encapsulating a-Si, which will affect the relative energies of competing surfaces. Incomplete rows of atoms along the surface facets, e.g., perpendicular to the red arrow in Figure 2a, can also be observed in NPs in S1 prior to heating.

In contrast to the predominately Ih NPs in S1, a wider variety of NP shapes could be seen in S2 (Figure 3), in contrast to theoretical predictions that show bulk-crystalline fcc structures are to be expected.[32,34] The size of the nanoparticles of the S2 sample is considerably greater than S1, which will play a dominant role in the change in stability of the different morphologies; however, the embedding a-Si layer is also thicker, and it could be possible that this thicker layer exerts an increased

constraining force on the particle. Although the thicker layer of embedding a-Si for S2 makes it extremely challenging to record HRTEM images and analyze the particle structures in detail, the variety of 2D outlines for NPs in Figure 3 clearly indicates that a range of structures are present. For consistency in our present work we focus our analysis of S2 only on the morphological changes that occur for the Ih NPs as the result of heating.

Upon heating the samples, we observed changes in nanoparticle morphologies: Figure 4 follows the outline of an Ih Ag NP in S2 with $d \approx 25$ nm, using TEM, as it is heated from RT to 1173 K. A minimal change in the NP structure is seen for $T < 773$ K; however, surface indentations appear at 873 K, and with further heating ($T > 923$ K) the sample starts to change shape and lose material, with the direction of loss of Ag atoms highlighted by the white arrows in Figure 4. The directionality of the Ag loss from the particle is remarkable and suggests that the atomic structure is of importance. Defects at the particle surface are likely to stimulate the detachment of Ag atoms until a perfect, uninterrupted atomic plane is formed: the presence of a defect makes the Ag diffusion or dissolution energetically possible, whereas the removal from a perfect plane requires much more energy. When the same *in situ* characterization was performed during heating of S1, focusing specifically on an Ih Ag NP with $d = 9.0$ nm (Figure 3, SI), we observed that material began to
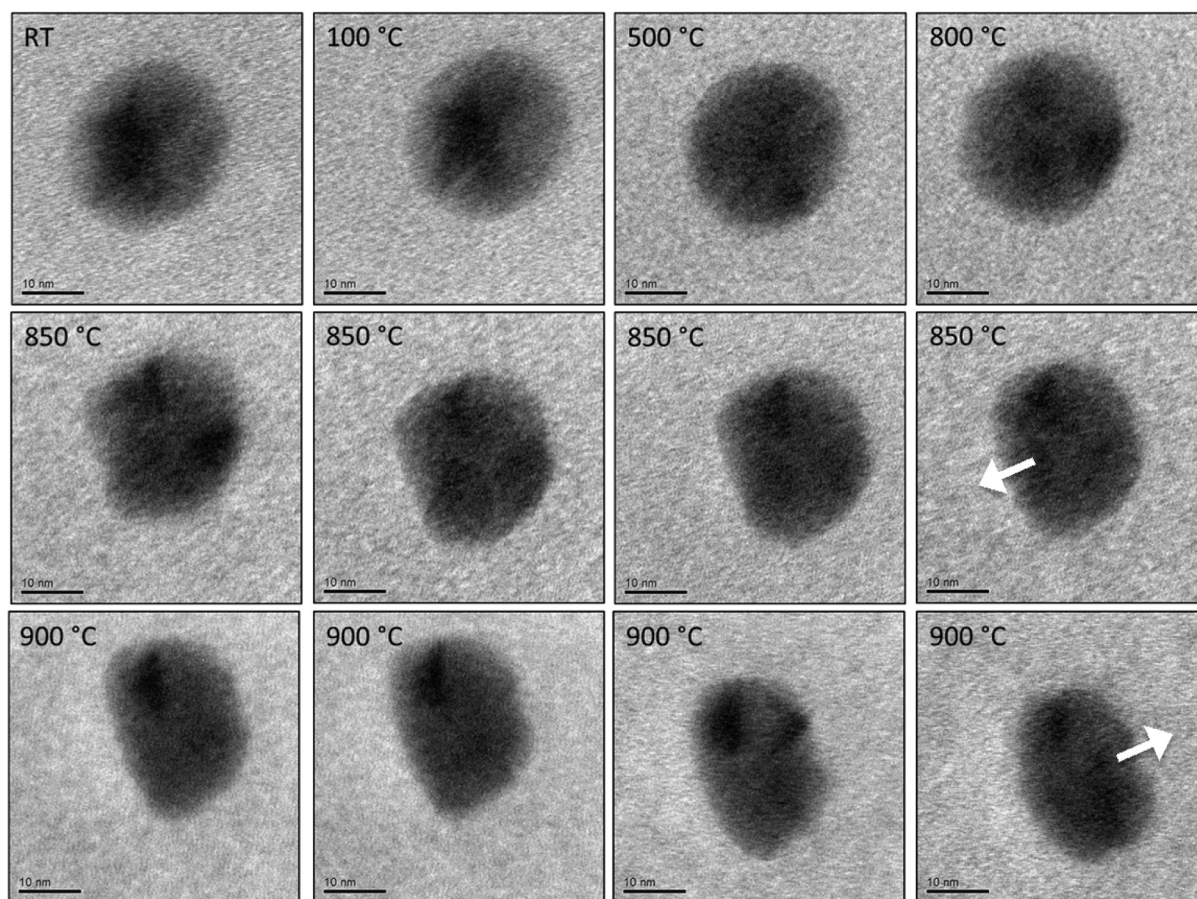
Figure 4. TEM images of a Ag nanoparticle ($d \approx 25$ nm) embedded in a-Si (Sample S2) as the sample is heated from room temperature (293 K) up to 1173 K. The temperature is provided in the top left of each image, along with a scale in the bottom left.
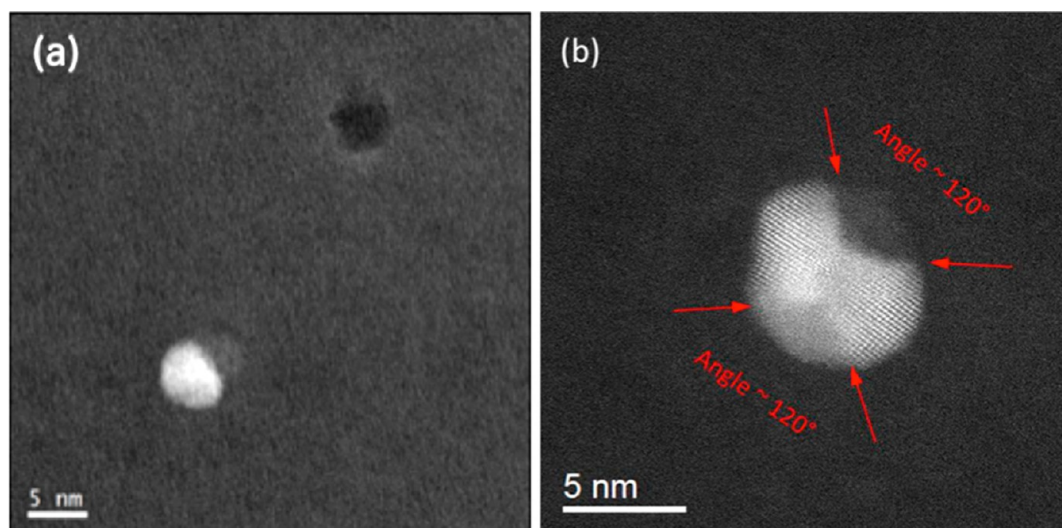
Figure 5. Postheating HAADF STEM images of Ag nanoparticles embedded in a-Si (Sample S1) at room temperature; the sample was heated to 773 K. Bright regions represent Ag atoms, gray regions the a-Si framework, and dark regions the voids. Areas where the Ag atoms have been removed are clearly visible in all images (a) and (b), with an entire nanoparticle removed in the top right of (a), leaving a dark void and a silver "halo" effect from the nearby embedded Ag atoms. A scale is provided in the bottom left of each image.

migrate out from the Ag NP for $T > 773$ K, i.e., at lower temperatures than in S2. For both samples, the NP size appears to decrease slightly during heating.

In order to understand better our observations, we examined the sample postheating using HAADF STEM, where diffraction contrast is negligible and image intensity is primarily dependent on the atomic number, Z, of an element.[19] Figure 5 presents HAADF STEM images of different Ag NPs from S1 at RT after annealing to 773 K; more images and analysis are provided in the SI. The following observations can be made: (i) a greater variety

of Ag NP morphologies are observed postheating than prior; (ii) parts of the Ag NPs disappear, leaving voids in the a-Si that are not observed during preheating (e.g., Figure 5b); (iii) Ag atoms remain present in the surrounding a-Si in a random arrangement, as confirmed using energy-dispersive spectroscopy (EDS), with the resulting Ag distribution visible as a "halo" in the HAADF STEM images (Figure 5a). Furthermore, the migration of the Ag atoms into or onto the a-Si matrix appears to be specific to certain parts of the NPs, as seen in Figure 5b (and Figures 4–6 in the SI). Particularly, the 120° angle between the remaining surface planes of the NP at the void is important, as it points to a strong relation between the crystal structure and detachment/dissolution of Ag atoms. The majority of voids in the a-Si matrix occur in S1 for NPs with $d < 5$ nm indicating a significant size dependence for the diffusion of parts of the Ag NPs.

The preferential detachment and subsequent diffusion of parts of the Ag NP, in some cases leaving voids in the a-Si structure, lead to several questions with respect to the properties of the Ag/a-Si system and specifically the Ag/a-Si interface. The Si–Ag phase diagram indicates that mixtures with high Ag concentrations result in a melting temperature (T_m) of ~1108 K,[35] illustrating the possibility of Ag/Si interfacial interdiffusion as found in research on solar cell applications,[36,37] though in general the mobility of Ag in Si is much lower than witnessed in our work.[26,27] A variation in the thermal stability depending on NP size is to be expected, given that previous work has shown that the melting temperature of Ag NPs increases with nanoparticle radius.[38–40] Although a systematic size dependence was not studied in this work, the change in T_m as observed by our simulations and experiments likely holds for a larger size range and therefore forms a qualitative explanation of the experimental results. For example, the melting temperature and subsequent detachment of silver atoms could be stimulated by the presence of structural defects. Surface imperfections, such as incomplete packing of surface atoms, are visible in some of our samples, with an example highlighted in Figure 2a by a red arrow.

Previous computations of melting in metallic NPs showed that superheating is possible in the absence of surface defects, when the NPs have well-defined clean boundaries,[41,42] and thus the interdiffusion of Ag and Si atoms is perhaps increased by surface defects. Explicit studies of atomic Ag migration into Si are limited to computational first-principles analysis of the Ag adsorption onto c-Si surfaces:[28,29] Julg and Allouche reported that "valley" sites (i.e., voids on the c-Si surface) were the most stable position for the adsorption of small Ag clusters, with an adsorption energy of 3.3 eV/atom, in agreement with experiment. Furthermore, it was also determined that the penetration of Ag atoms into the c-Si is impossible without considerable distortion energy,[28] due to the limited interspatial region between Si atoms; this finding was confirmed by Chou et al., who reported a penetration barrier for a Ag atom into a Si(111) surface of 2.30 eV, which is very large, for example compared to a barrier of 0.17 eV for Cu atoms.[29]

To understand the interdiffusion of Ag and Si in our experimental observations, we simulated the annealing of Ag NPs embedded in a-Si using NPT ensemble molecular dynamics calculations, where N, P, and T indicate constant moles, pressure, and temperature, respectively, in each step of the simulation. The embedded Ag NPs were constructed with 147 atoms (N), corresponding to a geometrically closed shell NP of $d \approx 1.5$ nm. The Ag NPs were modeled as both cuboctahedra (CO) and Ih, as these structures have different crystal packing and surface types but identical "closed-shell" geometric arrangements for $N = 147$: the CO, which is a bulk face-centered cubic (fcc) fragment, has 8

(100) surfaces and 6 (111) surfaces, whereas the Ih is a more tightly packed geometric motif with 20 (111) surfaces.[33,34] Upon initial heating, however, the CO performed a martensitic transformation to an Ih[43] at $T \approx 120$ K, as deduced from analysis of the Ag–Ag radial distribution function (RDF), which is presented in the SI; the transformation is due to the lower energy and, thus, higher stability of the Ih at small sizes. The martensitic transformation occurs at a significantly higher T in the equivalent gas-phase NPs, at $T \approx 230$ K, and so the lower transition T for the embedded Ag NP is attributed to the high internal strain of the nanoparticle, due to the unfavorable CO structure, being complemented with destabilization by the strong Ag–Si interactions: the Ag–Si interactions are 0.75 eV/atom stronger than the Ag–Ag interactions in our test calculations.

For $T > 400$ K, there is a significant decrease in the number of distinct peaks in the RDFs (Figure 6), from six to three, with the
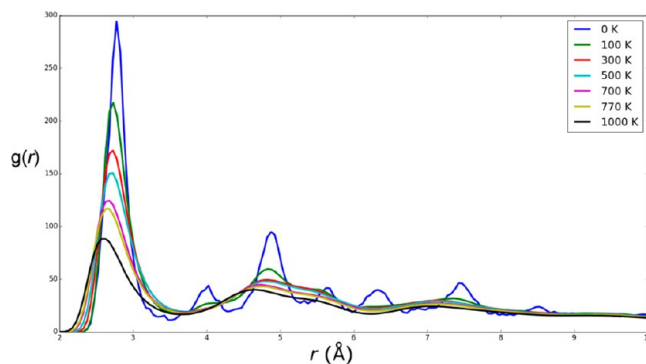
Figure 6. RDF of ensemble averaged Ag–Ag interactions within the Ag/a-Si system at 0, 100, 300, 500, 700, 770, and 1000 K, starting from Ag(CO) NPs embedded in a-Si. A key is provided.

remaining peaks shifted now to align with those of the Ih. At $T = 500$ K, we begin to see interdiffusion of Si and Ag atoms, with on average three Si atoms diffusing in to the Ag NPs, as documented in Table 1, which increases up to 12 (31) Si atoms within the Ag

Table 1. Summary of the Number of Si Atoms Inside Pristine Ag$_{147}$ (Defective Ag$_{134}$Si$_{13}$) NPs, Where the Definition of a Si Atom That Is Positioned Internally Is Defined as within the Outer Surface of the Ag NP

configuration	100 K	500 K	700 K	1000 K
1	0 (0)	3 (7)	11 (12)	31 (30)
2	0 (0)	3 (9)	10 (15)	32 (30)
3	0 (0)	3 (7)	13 (15)	32 (25)
4	0 (0)	2 (9)	5 (14)	28 (32)
5	0 (0)	1 (11)	14 (16)	32 (31)
6	0 (0)	4 (10)	13 (14)	31 (30)
7	0 (0)	3 (7)	9 (17)	27 (33)
8	0 (0)	3 (6)	15 (14)	31 (30)
9	0 (0)	3 (5)	8 (13)	28 (25)
10	0 (0)	8 (10)	18 (17)	37 (37)
mean	0 (0)	3 (8)	12 (15)	31 (30)

NP at $T = 700$ (1000) K, resulting in an increased amplitude for the Ag–Si RDF (Figure 14, SI). These calculations were compared to "defective" Ag NPs, where the 13 vertex atoms of the NPs were exchanged for Si atoms at the beginning of the simulations, and it was noted that Ag–Si interdiffusion was more prevalent in this case at $T = 500$ and 700 K, with on average 8 and

15 Si atoms in the Ag NPs, respectively (Table 1). Such an observation clearly indicates that increased interdiffusion of Ag and Si atoms can occur at low T when surface imperfections, such as defects, are present in the Ag NP. The observed mobility of Si atoms into the Ag NPs in the calculations is due to the weakness of the Ag–Ag interactions compared to the stronger Si–Si interactions (computed as 2.95 end 4.63 eV, respectively). The large thermodynamic energy barriers prevent distortion of the Si–Si bond, while the weaker Ag–Ag interactions allow the inclusion of Si atoms. This result perhaps suggests that the formation of the voids in a-Si in our experiment could alternatively be caused by diffusion of Ag atoms, which are detaching at their melting point, through microcracks toward the a-Si surface, as seen in Sample S2 (Figure 7, SI) or that the a-Si layer has some degree of porosity (microvoids), hosting the Ag atoms in pores.

Interestingly, when the influence of Si dopants on the melting temperature (T_m) of gas-phase Ag NPs was tested, single Si dopant atoms lowered the T_m from 890 K (Ag_{147}) to 599 K ($Ag_{146}Si$), whereas for 13 Si dopants the T_m increases again to 843 K ($Ag_{134}Si_{13}$), implying that small quantities of Si impurities could actually destabilize the Ag NPs while large quantities of Si impurities could stabilize the Ag NPs. This would have a strong effect on the dissolution of the larger Ag NPs (detachment of Ag atoms) seen in experiment: Si dopants stimulate localized melting and subsequent detachment of Ag surface atoms when present in low concentrations; in experiment, the sharp angles and planes of the Ag NPs, as well as the remaining complete Ag NPs, indicate that the process of melting and subsequent dissolution stops at a neighboring defect/dopant free atomic plane. In our simulations of the Ag/a-Si system, complete melting of the Ag NP was not witnessed; the preservation of order in the Ag–Ag RDF up to 1000 K for Ag/a-Si, well above the gas-phase T_m, indicates that the a-Si framework stabilizes the embedded Ag NPs.

CONCLUSIONS

In summary, we investigated pristine Ag NPs embedded in amorphous silicon upon heat treatment with *in situ* TEM and *ex situ* HRTEM and HAADF STEM. The morphological changes in these embedded Ag NPs during extended heating highlight the preferential diffusion of Ag atoms away from NPs of small sizes, especially in the presence of surface plane defects. Parts of the Ag NPs remain stable at elevated temperatures due to their "perfect" atomic planes that resist detachment of atoms. These observations are supported by ensemble molecular dynamics calculations, where incomplete geometric shells accelerated the interdiffusion of Ag and Si atoms upon annealing. The inclusion of Si atoms inside the Ag NP shows both stabilizing and destabilizing effects, depending on the Si dopant concentration, which explains why parts of the Ag NPs preferentially dissolve and other parts remain intact, as observed by the experiment. These results show that the intricate behavior of a metal NP inside a semiconductor matrix as a function of temperature can lead to different degrees of stability. The results are of relevance to optical coatings such as those used in solar cells, where the stability of the system is important.

ASSOCIATED CONTENT

Ⓢ Supporting Information

The Supporting Information is available free of charge on the ACS Publications website at DOI: 10.1021/acs.jpcc.5b07324.

Details of the experimental and computational simulations, covering topics such as support and nanoparticle morphology and stability, and accompanied by images and data (PDF)

AUTHOR INFORMATION

Corresponding Authors
*E-mail: a.logsdail@ucl.ac.uk
*E-mail: m.divece@uu.nl.

Author Contributions
The manuscript was written with contributions from all authors. SK, JBW, and MDV planned and performed all experimental work; ALG, CRAC, and AJL planned and performed all the computational simulations.

Notes
The authors declare no competing financial interest.

ABBREVIATIONS

NPs, nanoparticles; Ih, icosahedral; CO, cuboctahedral; fcc, face-centered cubic; c-Si, crystalline Si; a-Si, amorphous Si; TEM, transmission electron microscopy; HRTEM, high-resolution transmission electron microscopy; HAADF STEM, high-angle annular dark field scanning transmission electron microscopy; EELS, electron energy loss spectroscopy; EDS, electron dispersive spectroscopy; FFT, fast Fourier transform; E, energy; V, volume; T, temperature; RT, room temperature; NPT, isothermal–isobaric (constant moles, pressure and temperature); T_m, melting temperature; RDF, radial distribution function; SI, Supporting Information

REFERENCES

(1) Akimov, Y. A.; Koh, W. Resonant and Nonresonant Plasmonic Nanoparticle Enhancement for Thin-Film Silicon Solar Cells. *Nanotechnology* **2010**, *21*, 235201.

(2) Spinelli, P.; Hebbink, M.; De Waele, R.; Black, L.; Lenzmann, F.; Polman, A. Optical Impedance Matching Using Coupled Plasmonic Nanoparticle Arrays. *Nano Lett.* **2011**, *11*, 1760–1765.

(3) Spinelli, P.; Polman, A. Prospects of near-Field Plasmonic Absorption Enhancement in Semiconductor Materials Using Embedded Ag Nanoparticles. *Opt. Express* **2012**, *20*, A641–A654.

(4) Di Vece, M.; Kuang, Y.; van Duren, S. N.; Charry, J. M.; van Dijk, L.; Schropp, R. E. Plasmonic Nano-Antenna a-Si: H Solar Cell. *Opt. Express* **2012**, *20*, 27327–27336.

(5) Guo, C. F.; Sun, T.; Cao, F.; Liu, Q.; Ren, Z. Metallic Nanostructures for Light Trapping in Energy-Harvesting Devices. *Light: Sci. Appl.* **2014**, *3*, e161.

(6) Bhatt, K.; Tan, S.; Karumuri, S.; Kalkan, A. K. Charge-Selective Raman Scattering and Fluorescence Quenching by "Nanometal on Semiconductor" Substrates. *Nano Lett.* **2010**, *10*, 3880–3887.

(7) Sharma, B.; Frontiera, R. R.; Henry, A.-I.; Ringe, E.; Van Duyne, R. P. Sers: Materials, Applications, and the Future. *Mater. Today* **2012**, *15*, 16−25.

(8) Kadkhodazadeh, S.; Wagner, J. B.; Joseph, V.; Kneipp, J.; Kneipp, H.; Kneipp, K. Electron Energy Loss and One-and Two-Photon Excited Sers Probing of "Hot" Plasmonic Silver Nanoaggregates. *Plasmonics* **2013**, *8*, 763−767.

(9) Juluri, R.; Rath, A.; Ghosh, A.; Bhukta, A.; Sathyavathi, R.; Rao, D. N.; Müller, K.; Schowalter, M.; Frank, K.; Grieb, T. Coherently Embedded Ag Nanostructures in Si: 3d Imaging and Their Application to Sers. *Sci. Rep.* **2014**, DOI: 10.1038/srep04633.

(10) Ballif, C.; Huljić, D.; Willeke, G.; Hessler-Wyser, A. Silver Thick-Film Contacts on Highly Doped N-Type Silicon Emitters: Structural and Electronic Properties of the Interface. *Appl. Phys. Lett.* **2003**, *82*, 1878−1880.

(11) Li, Z.; Liang, L.; Cheng, L. Electron Microscopy Study of Front-Side Ag Contact in Crystalline Si Solar Cells. *J. Appl. Phys.* **2009**, *105*, 066102.

(12) Kuang, Y.; Di Vece, M.; Rath, J. K.; van Dijk, L.; Schropp, R. E. Elongated Nanostructures for Radial Junction Solar Cells. *Rep. Prog. Phys.* **2013**, *76*, 106502.

(13) Munday, J. N.; Atwater, H. A. Large Integrated Absorption Enhancement in Plasmonic Solar Cells by Combining Metallic Gratings and Antireflection Coatings. *Nano Lett.* **2010**, *11*, 2195−2201.

(14) Park, J.; Park, N.; Varlamov, S. Optimum Surface Condition for Plasmonic Ag Nanoparticles in Polycrystalline Silicon Thin Film Solar Cells. *Appl. Phys. Lett.* **2014**, *104*, 033903.

(15) Beck, F.; Polman, A.; Catchpole, K. Tunable Light Trapping for Solar Cells Using Localized Surface Plasmons. *J. Appl. Phys.* **2009**, *105*, 114310.

(16) Linic, S.; Christopher, P.; Ingram, D. B. Plasmonic-Metal Nanostructures for Efficient Conversion of Solar to Chemical Energy. *Nat. Mater.* **2011**, *10*, 911−921.

(17) Cassidy, C.; Singh, V.; Grammatikopoulos, P.; Djurabekova, F.; Nordlund, K.; Sowwan, M. Inoculation of Silicon Nanoparticles with Silver Atoms. *Sci. Rep.* **2013**, DOI: 10.1038/srep03083.

(18) Tao, A.; Sinsermsuksakul, P.; Yang, P. Tunable Plasmonic Lattices of Silver Nanocrystals. *Nat. Nanotechnol.* **2007**, *2*, 435−440.

(19) Li, Z.; Young, N.; Di Vece, M.; Palomba, S.; Palmer, R.; Bleloch, A.; Curley, B.; Johnston, R.; Jiang, J.; Yuan, J. Three-Dimensional Atomic-Scale Structure of Size-Selected Gold Nanoclusters. *Nature* **2008**, *451*, 46−48.

(20) Goris, B.; Bals, S.; Van den Broek, W.; Carbó-Argibay, E.; Gómez-Graña, S.; Liz-Marzán, L. M.; Van Tendeloo, G. Atomic-Scale Determination of Surface Facets in Gold Nanorods. *Nat. Mater.* **2012**, *11*, 930−935.

(21) Goris, B.; De Backer, A.; Van Aert, S.; Gómez-Graña, S.; Liz-Marzán, L. M.; Van Tendeloo, G.; Bals, S. Three-Dimensional Elemental Mapping at the Atomic Scale in Bimetallic Nanocrystals. *Nano Lett.* **2013**, *13*, 4236−4241.

(22) Chen, C.-C.; Zhu, C.; White, E. R.; Chiu, C.-Y.; Scott, M.; Regan, B.; Marks, L. D.; Huang, Y.; Miao, J. Three-Dimensional Imaging of Dislocations in a Nanoparticle at Atomic Resolution. *Nature* **2013**, *496*, 74−77.

(23) Fujita, T.; Tokunaga, T.; Zhang, L.; Li, D.; Chen, L.; Arai, S.; Yamamoto, Y.; Hirata, A.; Tanaka, N.; Ding, Y.; et al. Atomic Observation of Catalysis-Induced Nanopore Coarsening of Nanoporous Gold. *Nano Lett.* **2014**, *14*, 1172−1177.

(24) Raza, S.; Stenger, N.; Kadkhodazadeh, S.; Fischer, S. V.; Kostesha, N.; Jauho, A.-P.; Burrows, A.; Wubs, M.; Mortensen, N. A. Blueshift of the Surface Plasmon Resonance in Silver Nanoparticles Studied with Eels. *Nanophotonics* **2013**, *2*, 131−138.

(25) Logsdail, A. J.; Johnston, R. L. Predicting the Optical Properties of Core−Shell and Janus Segregated Au−M Nanoparticles (M= Ag, Pd). *J. Phys. Chem. C* **2012**, *116*, 23616−23628.

(26) Coffa, S.; Poate, J.; Jacobson, D.; Frank, W.; Gustin, W. Determination of Diffusion Mechanisms in Amorphous Silicon. *Phys. Rev. B: Condens. Matter Mater. Phys.* **1992**, *45*, 8355.

(27) Nason, T.; Yang, G. R.; Park, K. H.; Lu, T. M. Study of Silver Diffusion into Si (111) and Sio2 at Moderate Temperatures. *J. Appl. Phys.* **1991**, *70*, 1392−1396.

(28) Julg, A.; Allouche, A. Theoretical Study of the Adsorption of Silver Atoms on the (111) Face of Silicon. *Int. J. Quantum Chem.* **1982**, *22*, 739−752.

(29) Chou, S. H.; Freeman, A.; Grigoras, S.; Gentle, T.; Delley, B.; Wimmer, E. Bonding of Noble Metals to Semiconductor Surfaces: First-Principles Calculations of Copper and Silver on Silicon (111). *J. Am. Chem. Soc.* **1987**, *109*, 1880−1881.

(30) Haberland, H.; Mall, M.; Moseler, M.; Qiang, Y.; Reiners, T.; Thurner, Y. Filling of Micron-Sized Contact Holes with Copper by Energetic Cluster Impact. *J. Vac. Sci. Technol., A* **1994**, *12*, 2925−2930.

(31) Wegner, K.; Piseri, P.; Tafreshi, H. V.; Milani, P. Cluster Beam Deposition: A Tool for Nanoscale Science and Technology. *J. Phys. D: Appl. Phys.* **2006**, *39*, R439.

(32) Ling, T.; Xie, L.; Zhu, J.; Yu, H.; Ye, H.; Yu, R.; Cheng, Z.; Liu, L.; Yang, G.; et al. Icosahedral Face-Centered Cubic Fe Nanoparticles: Facile Synthesis and Characterization with Aberration-Corrected Tem. *Nano Lett.* **2009**, *9*, 1572−1576.

(33) Baletto, F.; Ferrando, R. Structural Properties of Nanoclusters: Energetic, Thermodynamic, and Kinetic Effects. *Rev. Mod. Phys.* **2005**, *77*, 371.

(34) Baletto, F.; Ferrando, R.; Fortunelli, A.; Montalenti, F.; Mottet, C. Crossover among Structural Motifs in Transition and Noble-Metal Clusters. *J. Chem. Phys.* **2002**, *116*, 3856−3863.

(35) Olesinski, R.; Gokhale, A.; Abbaschian, G. The Ag-Si (Silver-Silicon) System. *Bull. Alloy Phase Diagrams* **1989**, *10*, 635−640.

(36) Rollert, F.; Stolwijk, N.; Mehrer, H. Solubility, Diffusion and Thermodynamic Properties of Silver in Silicon. *J. Phys. D: Appl. Phys.* **1987**, *20*, 1148.

(37) McBrayer, J. D.; Swanson, R.; Sigmon, T. Diffusion of Metals in Silicon Dioxide. *J. Electrochem. Soc.* **1986**, *133*, 1242−1246.

(38) Luo, W.; Hu, W.; Xiao, S. Size Effect on the Thermodynamic Properties of Silver Nanoparticles. *J. Phys. Chem. C* **2008**, *112*, 2359−2369.

(39) Couchman, P.; Jesser, W. *Nature* **1977**, *269*, 481−483.

(40) Asoro, M.; Damiano, J.; Ferreira, P. Size Effects on the Melting Temperature of Silver Nanoparticles: In-Situ Tem Observations. *Microsc. Microanal.* **2009**, *15*, 706−707.

(41) Schebarchov, D.; Hendy, S. Static, Transient, and Dynamic Phase Coexistence in Metal Nanoclusters. *J. Chem. Phys.* **2005**, *123*, 104701.

(42) Schebarchov, D.; Hendy, S. Superheating and Solid-Liquid Phase Coexistence in Nanoparticles with Nonmelting Surfaces. *Phys. Rev. Lett.* **2006**, *96*, 256101.

(43) Chen, F.; Johnston, R. L. Martensitic Transformations in Ag−Au Bimetallic Core-Shell Nanoalloys. *Appl. Phys. Lett.* **2008**, *92*, 023112−023112−3.